JACS
JOURNAL OF THE AMERICAN CHEMICAL SOCIETY
pubs.acs.org/JACS
Article

Structural Insights into the Mechanism of High-Affinity Binding of Ochratoxin A by a DNA Aptamer

Guohua Xu, Jiajing Zhao, Hao Yu, Chen Wang, Yangyu Huang, Qiang Zhao,* Xin Zhou, Conggang Li,* and Maili Liu

Cite This: J. Am. Chem. Soc. 2022, 144, 7731−7740
Read Online

ABSTRACT: A 36-mer guanine (G)-rich DNA aptamer (OBA36) is able to distinguish one atomic difference between ochratoxin analogues A (OTA) and B (OTB), showing prominent recognition specificity and affinity among hundreds of aptamers for small molecules. Why OBA36 has >100-fold higher binding affinity to OTA than OTB remains a long-standing question due to the lack of high-resolution structure. Here we report the solution NMR structure of the aptamer−OTA complex. It was found that OTA binding induces the aptamer to fold into a well-defined unique duplex−quadruplex structural scaffold stabilized by Mg^{2+} and Na^{+} ions. OTA does not directly interact with the G-quadruplex, but specifically binds at the junction between the double helix and G-quadruplex through $\pi-\pi$ stacking, halogen bonding (X-bond), and hydrophobic interaction. OTB has the same binding site as OTA but lacks the X-bond. The strong X-bond formed between the chlorine atom of OTA and the aromatic ring of C5 is the key to discriminating the strong binding toward OTA. The present research contributes to a deeper insight of aptamer molecular recognition, reveals structural basis of the high-affinity binding of aptamers, and provides a foundation for further aptamer engineering and applications.

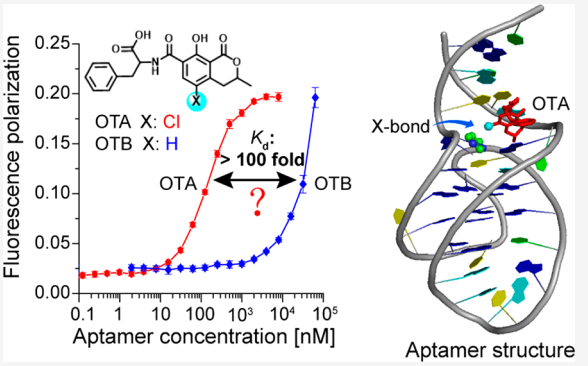

INTRODUCTION

Aptamers are short single-stranded oligonucleotides that are generated via the SELEX method (Systematic Evolution of Ligands by EXponential enrichment) to bind various targets from small molecules to protein, and even whole cells, with high affinity and specificity. Aptamers have diverse and increasing applications in biosensors, disease diagnosis, affinity separation, therapeutics, and drug delivery.[1−10] To date, aptamers have become powerful tools to analyze and detect small molecules, as hundreds of aptamers have been isolated for a number of small-molecule targets, such as biomarkers, drugs, pollutants, cofactors, toxins, and metabolites.[3,4,11−17]

Ochratoxin A (OTA) (Figure 1), a derivative of isocumarin linked via a peptide bond with L-phenylalanine, is a widespread food-contaminating small-molecule mycotoxin mainly produced by fungal species *Aspergillus ochraceus* and *Penicillium verrucosum*. OTA poses a serious health threat to both humans and animals due to its nephrotoxicity and carcinogenicity,[18−20] which makes the detection of OTA important for food safety, environment monitoring, and risk assessment.

The discovery of OTA aptamers allows for aptamer-based biosensors, assays, and affinity extractions for OTA, overcoming limitations of immunoantibodies.[4,21−23] A 36-mer guanine (G)-rich OTA-binding DNA aptamer (OBA36) with the sequence 5′-GATCGGGTGTGGGTGGCGTAAAGGGAGCATCGGACA-3′, selected by Cruz-Aguado et al.[24] in 2008, is one of the prominent aptamers among hundreds of aptamers for small molecules due to its great binding performances, drawing increasing and intense attention.[4,21,22] OBA36 is able to distinguish one atomic difference between OTA and OTB, which is a nonchlorinated structural analogue of OTA (the chlorine in the isocoumarin ring of OTA is a hydrogen in OTB). OBA36 binds OTA with a dissociation constant (K_d) down to ∼50 nM (the K_d value may slightly vary depending on buffer conditions and analytical methods used), but binds OTB with more than 100-fold reduced affinity compared to OTA.[24,25] Why OBA36 has superior binding affinity and specificity is a long-standing question in the aptamer research field.

Low-resolution circular dichroism (CD) spectroscopy shows the aptamer folds into an antiparallel G-quadruplex (GQ) structure in the absence and presence of OTA.[26] GQ topology structure was further determined by the method in which

Received: January 17, 2022
Published: April 20, 2022

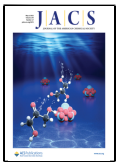

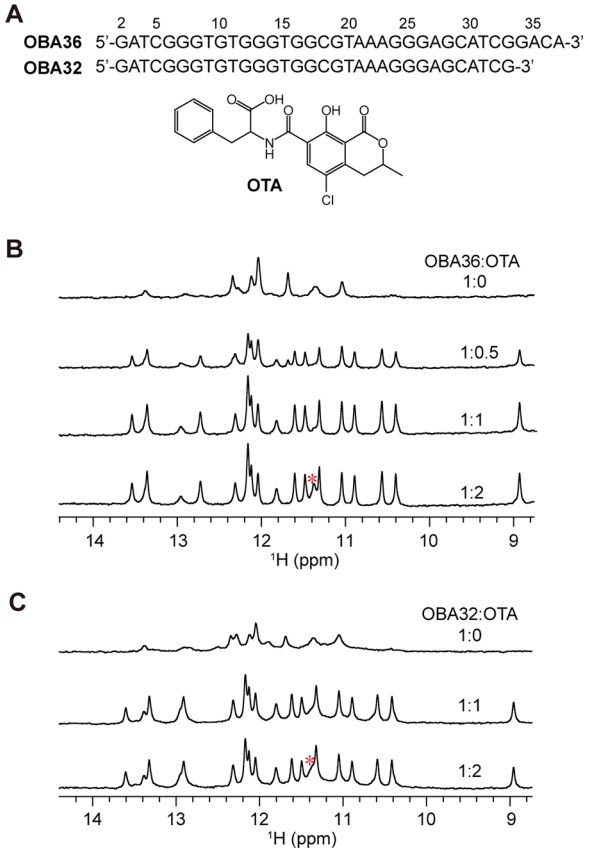

Figure 1. ^{1}H NMR spectra of the aptamers. (A) Sequence of aptamers OBA36 and OBA32 and chemical structure of OTA. The sequence numbering of OBA36 and OBA32 starts with number 2 for the consistent numbering of all the constructs in the article. (B, C) Imino regions of ^{1}H NMR spectra of OBA36 and OBA32 aptamers titrated with OTA in 10 mM Na_2HPO_4/KH_2PO_4 buffer (pH 7.4) containing 120 mM NaCl, 10 mM KCl, and 10 mM $MgCl_2$, at 288 K, respectively. The asterisk indicates the peak from the proton of free OTA.

fluorescent nucleobase analogue 8-thienyl-2′-deoxyguanosine (ThdG) was inserted into various G sites of the aptamer, and OTA was thought to insert between the G-tetrad residues.[27,28] In addition, metal ions play crucial roles in the binding of OTA to the aptamer because both the aptamer and OTA are negatively charged, and the direct interaction between them is difficult. The binding of OTA to the aptamer highly depends on the presence of divalent cations whose removal causes the loss of binding affinity, whereas the removal of Na^+ and K^+ just induces a 20-fold decrease of binding affinity.[24,25] However, it is still not clear about the structural basis for high-affinity and -specificity binding of this aptamer and the detailed functions of these metal ions in aptamer−OTA binding.

Determination of high-resolution structure is an effective way to answer these questions. Herein, we solved the high-resolution solution structures of an OTA-bound high-affinity aptamer by NMR spectroscopy and revealed the molecular mechanism of high-affinity and -specificity recognition of OTA by aptamers and detailed ion function. The study will really contribute to the design and improvement of aptamers and aptamer-based biosensors and the interpretation of the mechanism of OTA toxicity.

MATERIALS AND METHODS

Sample Preparation. Ochratoxins A and B were purchased from Aladdin (Shanghai, China) and J&K Scientific (Beijing, China), respectively, and the ochratoxins were dissolved in d_6-DMSO as stock solutions for further use. DNA oligos were synthesized by Sangon Biotechnology Co., Ltd. (Shanghai, China). NMR samples were prepared by dissolving the lyophilized DNA powder in either D_2O or 9:1 H_2O/D_2O containing 10 mM Na_2HPO_4/NaH_2PO_4, 120 mM NaCl, 5 mM KCl, and 10 mM $MgCl_2$, pH 7.4, or dissolving DNA in 9:1 H_2O/D_2O containing 10 mM Tris-HCl with various ions. The concentration of nucleic acids for NMR samples was 0.05−2 mM.

NMR Spectroscopy. NMR spectra were recorded on Bruker 600, 700, and 850 MHz NMR spectrometers equipped with a CyroProbe, at 288 and 308 K, respectively. 2D ^{1}H−^{1}H TOCSY (120 ms mixing time) and DQF-COSY spectra were acquired in D_2O with 512 complex points in the t1 dimension and 2048 in the t2 dimension. 2D ^{1}H−^{1}H NOESY spectra were collected in D_2O and 10% D_2O, respectively, with mixing times of 120, 300, and 500 ms and 256−512 complex points in the t1 dimension and 2048 in the t2 dimension. ^{1}H chemical shifts were referenced to 2,2-dimethylsilapentane-5-sulfonic acid (DSS) at 0 ppm. The 2D JR-HMBC spectrum[29] was collected with 56 complex points along the t1 dimension and 2048 points along the t2 dimension, with 10K scans at 288 K. Both 2D ^{31}P−^{1}H COSY[30] and HSQC[31] were recorded at 308 K. ^{31}P chemical shifts were referenced to an external standard of 85% H_3PO_4. All NMR spectra were processed using Bruker TopSpin software and analyzed using the software Sparky.[32]

Structure Calculation. The structures of the OBA33−OTA complex were calculated following the standard protocol[33] using Xplor-NIH 2.47,[34,35] as described previously.[36] Hydrogen bonding and NOE distance restraints, dihedral angles restraints including glycosidic dihedral angles (χ), and sugar backbone dihedral angles β, γ, and ε were used in the calculation. Distance restraints were mainly based on NOESY spectra with a mixing time of 120 ms. A total of 200 structures were obtained, and the 10 lowest energy structures were chosen for further analysis. Structures were analyzed and displayed using PyMOL Molecular Graphics System, version 0.99rc6, Schrödinger, LLC.

Fluorescence Polarization Analysis. Fluorescence polarization (FP) of OTA was measured with a Jasco FP-8300 fluorescence spectrometer (Japan) at room temperature (298 K) as described previously.[25] The buffer for FP experiments was 10 mM Tris-HCl (pH 7.5) containing 10 mM $MgCl_2$, 120 mM NaCl, and 5 mM KCl, containing 10 mM $MgCl_2$ and 120 mM NaCl, or containing 10 mM $MgCl_2$ and 5 mM KCl, and 0.1% Tween 20. The fixed concentration of OTA or OTB was 50 nM in a 100 μL quartz cuvette. FP was measured with excitation at 375 nm and emission at 440 nm and a slit of 5 nm. Five data points were collected, and the averaged value was used for data processing.

Isothermal Titration Calorimetry (ITC) Analysis. Characterization of affinity binding between aptamers and OTA with ITC was conducted by using a Microcal PEAQ-ITC microcalorimeter (Malvern). Aptamers and OTA solutions were prepared in a buffer of 10 mM Tris-HCl (pH 7.5), 10 mM $MgCl_2$, 120 mM NaCl, 5 mM KCl, and 2% DMSO. In ITC measurements, 50 μM OTA in the injection syringe was titrated into 5 μM aptamer in a sample cell at 25 °C. After an initial 60 s equilibration, the experiments started with the first 0.4 μL of OTA solution and 19 successive 2.0 μL of OTA solution every 100 s with the syringe stirring speed of 750 rpm. The reference power was set as 10 μcal/s. By integrating the heat pulse area of each titration, the titration curves were obtained. Dissociation constant (K_d), binding stoichiometry (N), enthalpy change (ΔH), free energy change (ΔG), and entropy change ($T\Delta S$) were determined from the MicroCal PEAQ-ITC analysis software.

Circular Dichroism Spectroscopy. CD samples were prepared by dissolving 10 μM aptamer in a 10 mM Tris-HCl (pH 7.5) buffer containing $Mg^{2+}/Na^+/K^+$, Mg^{2+}/Na^+, or Mg^{2+}/K^+ in the presence of two equivalents of OTA. The concentrations of ions are the same as that in FP experiments. CD spectra were registered on a Chiriscan

https://doi.org/10.1021/jacs.2c00478
J. Am. Chem. Soc. 2022, 144, 7731−7740

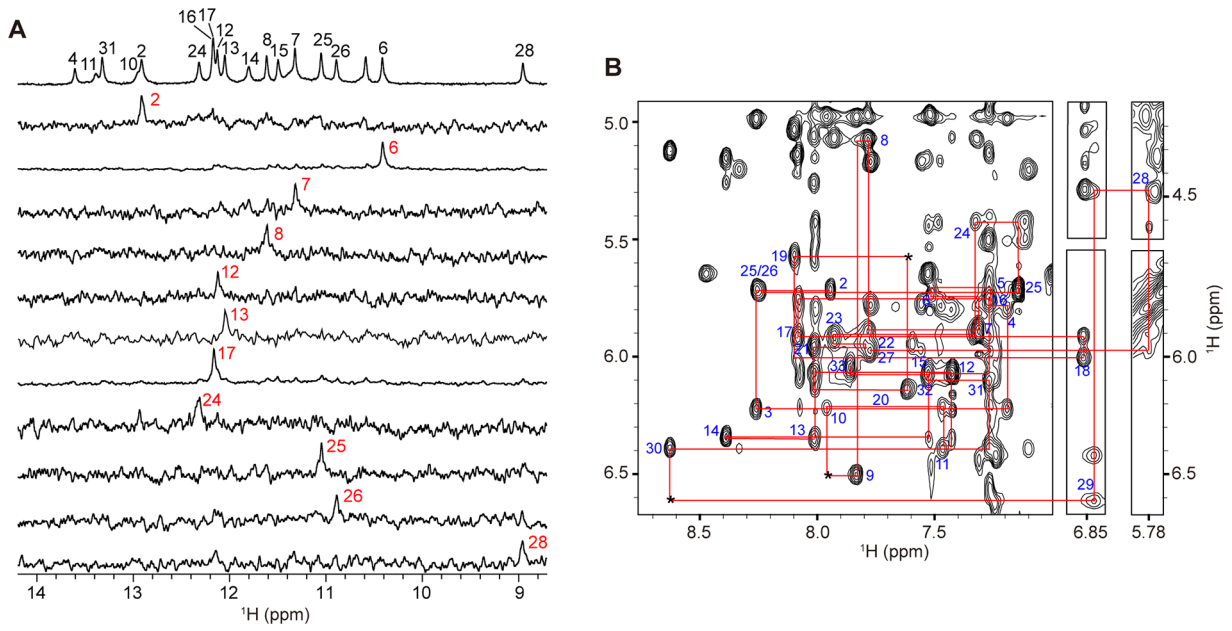

Figure 2. Assignments of the OBA32−OTA complex. (A) Imino proton spectra of the OBA32−OTA complex. Imino protons were assigned from ^{15}N-filtered spectra of samples, 2.5% ^{15}N site-specific-labeled at indicated positions. (B) NOESY spectrum of the OBA32−OTA complex in H_2O (mixing time, 300 ms), showing the H8/6-H1′ sequential connectivities. Intraresidue H8/6-H1′ cross-peaks are labeled with residue numbers. Missing connectivities are marked with asterisks.

circular dichroism photomultiplier (Applied Photophsics Limited. UK). For the CD spectra, the wavelength was varied from 220 to 320 nm at room temperature. Each trace is the result of a step size of 1 nm, a time per point of 0.5 s, and a bandwidth of 1 nm.

RESULTS

Stoichiometry Determination of OBA and OTA Complexes. Aptamers were selected by SELEX in buffer containing 120 mM NaCl and 5 mM KCl (high Na^+ and low K^+ ion buffer) in the presence of divalent Mg^{2+} or Ca^{2+} ions.[24] Therefore, we first acquired ^{1}H NMR spectra of OBA36 in NMR buffer containing 10 mM Na_2HPO_4/NaH_2PO_4, 120 mM NaCl, 5 mM KCl, and 10 mM $MgCl_2$, pH 7.4 ($Mg^{2+}/Na^+/K^+$ buffer) (Figure 1). NMR spectra of imino protons of aptamers are very sensitive to aptamer structure. In the absence of OTA, the imino protons of free OBA36 display some broad resonances in the 10−14 ppm range, suggesting that free OBA36 may form G-quadruplex and duplex conformations,[37] but it lacks a defined and stabilized structure. Upon the addition of OTA, the spectral line widths become obviously narrowed, and meanwhile several new resonances appear in the 10−14 ppm range, indicating the formation of a well-defined structure containing G-quadruplex and double-helix conformations. Compared to the ^{1}H NMR spectrum with one equivalent of OTA, there is no change when the two equivalents of OTA were added, suggesting a 1:1 stoichiometry. The consistent stoichiometry result was also obtained using ITC (Figure S1).

OBA32 (5′-GATCGGGTGTGGGTGGCGTAAAGGGAG-CATCG-3′), the 3′-end 4-nt truncated aptamer of OBA36, is the shorter sequence whose affinity binding to OTA was maintained effectively.[24,25] NMR spectra show that OBA32 gave rise to quite similar signals to OBA36 both for the free aptamers and when bound to OTA (Figure 1), implying that the 3′-end 4-nt of O36 is negligible for aptamer recognition. For NMR structure determination, a shorter aptamer sequence is easier to analyze spectrally due to the decreased number of signal peaks. Therefore, we determined the solution structures of the OTA-bound OBA32 aptamer.

Folding Topology of the OBA32−OTA Complex. Guanine imino (H1) and aromatic (H8) protons of OBA32 were assigned by ^{15}N site-specific low-enrichment labeling (Figure 2) and through-bond correlations between imino and H8 protons via ^{13}C at natural abundance (Figure S2). With the help of these assignments and other NMR experiments (COSY and TOCSY), the H8/6-H1′ NOE sequential connectivity can be traced for almost all nucleobases (Figure 2). For nucleobases missing H8/6-H1′ NOE sequential connectivities, H8/6-H2′/2″/3′ NOE sequential connectivities were used to confirm assignments.

The folding topology of OBA32 in the complex was determined by analyzing the NOEs between the imino (H1) and other protons (Figure 3). The characteristic imino-H8 proton cyclic NOE connectivity patterns around G-tetrads (Figure 3A,B) established a two-layered chair-type antiparallel G-quadruplex structure involving G7·G26·G16·G13 and G8·G12·G17·G25 tetrads (Figure 3C), consistent with the previous study.[28] The glycosidic conformations of the G-tetrads are *syn·anti·syn·anti* and *anti·syn·anti·syn*, respectively, which are reflected by H8−H1′ NOE cross-peak intensities of these residues in NOESY spectra. In the two G-tracts of the G-tetrad core, G7-G8 and G16-G17 are in one direction and the other two G-tracts, G12-G13 and G25-G26, are in the opposite direction. The structure has three edgewise loops, i.e., the first 3-nt loop T9-G10-T11, the second 2-nt loop G14-T15, and the third 7-nt loop C18-G19-T20-A21-A22-A23-G24. The G·G·C triple forms between the G10 in the first loop and the G24 and C18 in the third loop, which is supported by the strong NOEs G10H1/G24H8 and G24H1/C18H41 (Figure 3A,B). The reversed Hoogsteen A·T base pair as shown in Figure 3B forms between the T11 in the first loop and the A23 in the third loop, which is supported by the strong NOEs T11H3/A23H8 (Figure 3A).

https://doi.org/10.1021/jacs.2c00478
J. Am. Chem. Soc. 2022, 144, 7731−7740

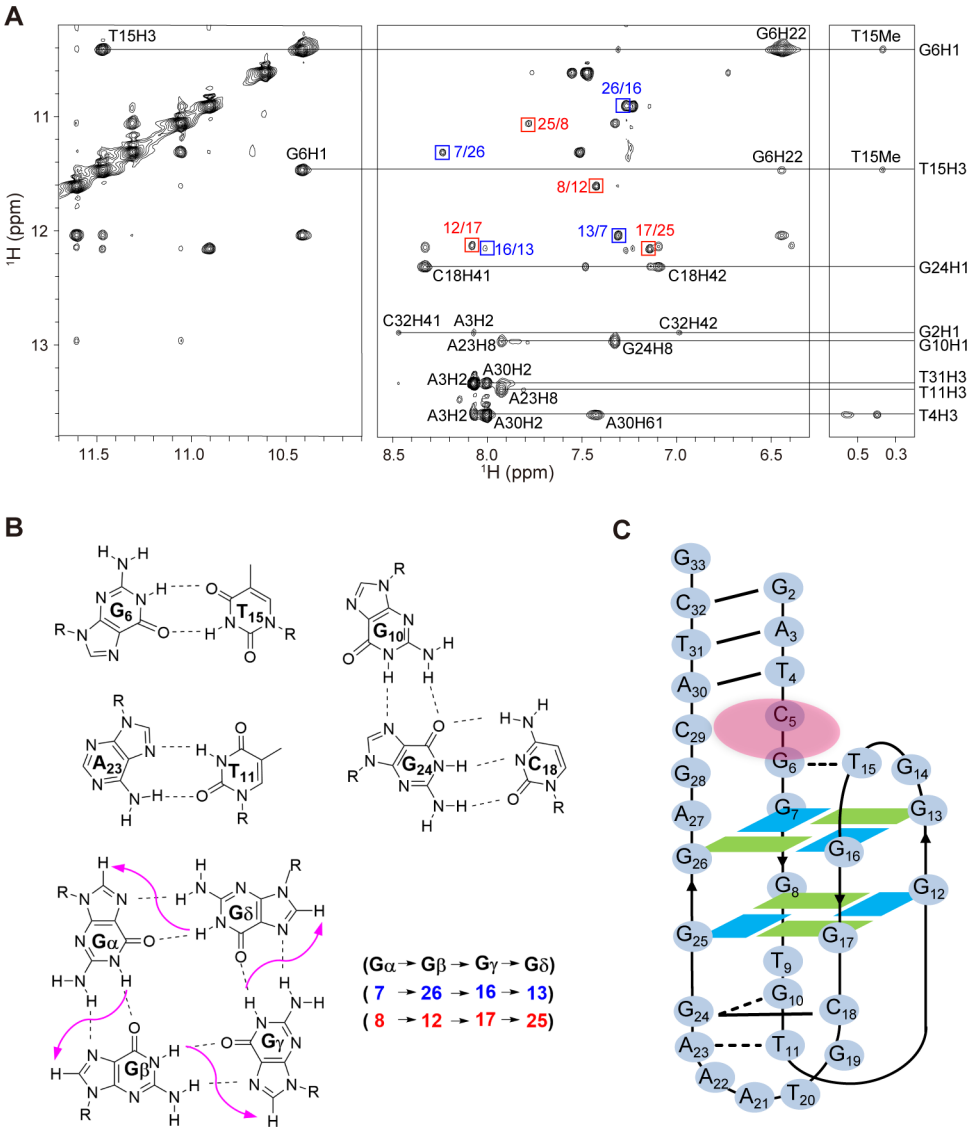

Figure 3. Global topology of the OBA32−OTA complex deduced from NOESY spectra. (A) Expanded NOESY spectrum (mixing time, 300 ms) of the OBA32−OTA complex in H_2O buffer at 288 K, correlating NOEs between the imino protons and the amino and base protons. The arrangements of G-tetrads were identified from framed cross-peaks with the residue number of imino protons labeled in the first position and that of H8 protons in the second position. (B) Schematic representation of G-tetrads, G·G·C triple, and reversed wobble G·T, A·T reversed Hoogsteen base pairs observed in the NOESY spectrum of the OBA32−OTA complex. Characteristic guanine imino-H8 proton NOE connectivity patterns around G-tetrads are shown in the magenta row. (C) Schematic structure of the OBA32−OTA complex satisfying the NOE connectivities. *Anti* and *syn* guanines in G-tetrads are colored blue and cyan, respectively. OTA is shown as the pink ellipse.

The bases G2-A3-T4 and A30-T31-C32 form a duplex structure by canonical G·C and A·T Watson−Crick pairing (G2·C32, A3·T31, T4·A30 pairs), which are supported by the strong NOEs between the imino proton of the G base and the amino protons of the C base and between the imino proton of the T base and the H2 proton of the A base (Figure 3). The base G6 forms a reversed wobble G·T pair with T15, as shown in Figure 3B, which is supported by strong NOEs G6H1/T15H3. The terminal G33 base does not pair.

Following the unambiguous assignment of proton resonances of OBA32 and OTA, we also identified the intermolecular NOEs between the protons of OTA and T4, T15, A27, G28, C29, and A30, indicating that OTA binds in the pocket composed of these nucleotides and does not directly bind to the G-quadruplex region. Figure 3C shows the schematic structure of the OBA32−OTA complex satisfying the above NMR-determined NOE connectivities, from which it can be deduced that the 3′-end 4 nt of OBA36 does not pair to form a structure or directly participate in binding to OTA, explaining why OBA32 and OBA36 exhibit similar NMR spectroscopy and binding affinities.

Solution Structure of the OBA33−OTA Complex. As shown in Figure 3C, the terminal G33 base lacks a complementary base in the OBA32−OTA complex, which likely reduces the binding affinity of the aptamer to OTA according to our previous research.[36] Therefore, we tried to add a C to the 5′-terminus of OBA32 to generate a new OBA33 aptamer with one more G·C pair compared to OBA32 to enhance the stem stability. We then employed fluorescence polarization to determine the binding affinity to OTA in the presence of Mg^{2+} (Figure S3, Table S1). OBA33 shows a slightly improved affinity (54 ± 2 nM) compared to OBA32

https://doi.org/10.1021/jacs.2c00478
J. Am. Chem. Soc. 2022, 144, 7731−7740

(67 ± 3 nM) (Table S1). Due to the superior spectral quality of OBA33, which helps identify some ambiguous assignments in the OBA32−OTA complex, we recorded a series of NMR spectra of the OBA33−OTA complex and determined the solution high-resolution structure of the OBA33−OTA complex. The proton resonances of the OBA33−OTA complex were assigned in a similar way to the OBA32−OTA complex (Table S2). Figure S4 shows the H8/6-H1′ sequential connectivities and the correlation of imino protons with amino/base protons of the OBA33−OTA complex, respectively.

The solution structure of the OBA33−OTA complex was calculated using NMR restraints including intramolecular and intermolecular NOEs, hydrogen bonds, and dihedral angles (Table S3). The lowest-energy refined structures of the complex are presented in Figure 4. The structures are well-defined with the average pairwise RMSD value of 0.57 ± 0.14 Å for all heavy atoms of the entire complex (Table S3).

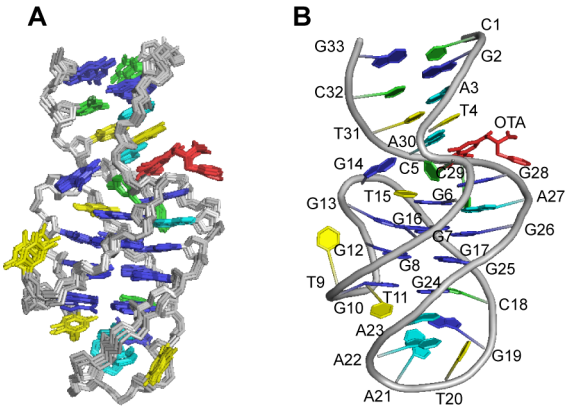

Figure 4. Solution structure of the OBA33−OTA complex. (A) Ten superimposed refined structures. (B) Cartoon view of a representative refined structure. Guanines are colored blue; cytosines, green; adenines, cyan; thymines, yellow; backbone and sugars, gray; OTA, red.

Like the OBA32−OTA complex, the OBA33−OTA complex forms a duplex−quadruplex structural scaffold (Figures 4 and 5). The G10·G24·C18 triple and noncanonical A23·T11 pair between two loops (the first loop: T9-G10-T11 3-nt loop; the third loop: C18-G19-T20-A21-A22-A23-G24 7-nt loop) stack well with the G-quadruplex core, helping to stabilize the G-quadruplex fold. We also observed the formation of the G19·A22 pair in the 7-nt loop, although the hydrogen bond restraints between them were not used in structure calculations due to the fact that the resonances of the NH_2 group of G19 and A22 were not observed in the NMR spectra. The G19·A22 pair is likely to help stabilize the third loop and further G-quadruplex structure.

Binding Pocket Architecture. OTA binds at the junction between the duplex and G-quadruplex of the complex (Figure 6). OTA does not directly interact with the G-quadruplex, which is not consistent with the previous prediction.[28] The residues C5, G6, T15, A27, G28, and C29, which form the base quartet G6·T15·A27·C29 and triplet C5·T15·G28 by hydrogen bonding (Figure 6A,B), the residue G14, which forms hydrogen bonds by its H1 and NH_2 with phosphate oxygens O1P of C5 and phosphodiester oxygens O3′ of T4, respectively (Figure 6B), and the residues T4 and A30, which form a T4·A30 Watson−Crick pair, building the OTA binding pocket. OTA is anchored mainly by the stacking of the isocoumarin ring of OTA between the T4·A30 base pair and the G28 base (Figure 6C), the halogen bonds between the chlorine atom of OTA and aromatic ring of the C5 base (Figure 6D), and the hydrophobic interactions between the methyl group of OTA and C29 and between the benzene ring of OTA and sugar rings of A27 and G28 (Figure 6E).

The halogen bond (X-bond) plays an important role in the recognition of the aptamer by OTA. A halogen bond is a directional noncovalent interaction between a halogen atom and electron donor.[38,39] The electron density donors are usually represented by electronegative atoms such as oxygen, nitrogen, or sulfur and also by aromatic rings or conjugated π-systems. Nucleic acids are prospective X-bond acceptors because they are naturally rich in electronegative atoms. Herein the potential X-bonds between the chlorine atom of OTA and aptamer were searched according to the criteria that the distance between the halogen and electronegative atoms (O, N, P) is shorter than 4.2 Å and the angle R−X···O/N/P is higher than 120°, or the perpendicular distance between the halogen atom and the aromatic ring plane is shorter than 4.2 Å and the angle between the R−X bond and plane normal vector is smaller than 60°. It was found that the strong halogen bond forms between the chlorine atom of OTA and aromatic ring of

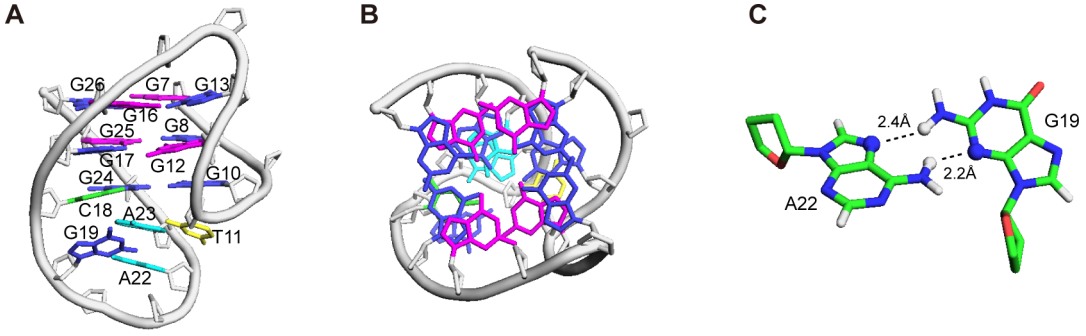

Figure 5. Expanded view of an antiparallel G-quadruplex in one representative OBA33−OTA complex structure. (A, B) Side (A) and top (B) view of the G13·G7·G26·G16 tetrad, G12·G17·G25·G8 tetrad, G10·G24·C18 triple, and A23·T11 pair between two loops (T9-G10-T11 3-nt loop and C18-G19-T20-A21-A22-A23-G24 7-nt loop) and G19·A22 pair in the 7-nt loop segment in the antiparallel G-quadruplex. Cytosines are colored green; adenines, cyan; thymines, yellow; backbone and sugars, gray. *Anti* and *syn* guanines are colored blue and magenta, respectively. (C) Hydrogen-bonding alignments of the G19·A22 pair. Oxygen, nitrogen, carbon, and hydrogen atoms are depicted in red, blue, green, and gray, respectively.

https://doi.org/10.1021/jacs.2c00478
J. Am. Chem. Soc. 2022, 144, 7731−7740

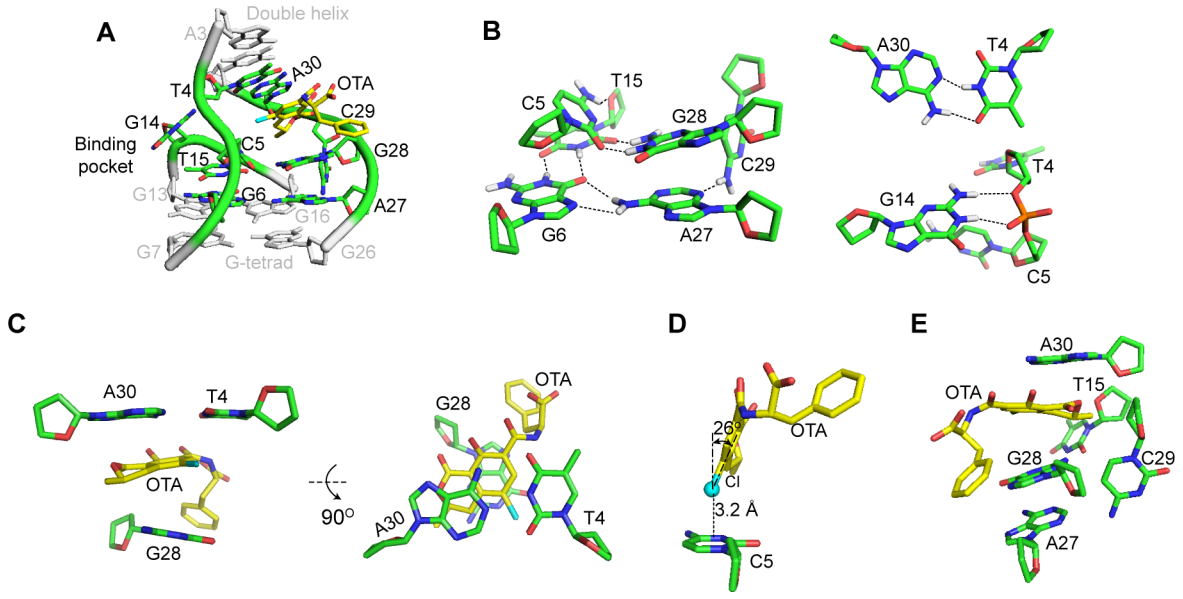

Figure 6. Structural details of the OTA binding site in one representative OBA33−OTA complex structure. (A) Side view showing the OTA binding pocket. (B) Hydrogen-bonding alignments of the bases within the binding pocket. (C) Side and top view showing the stacking of the isocoumarin ring of OTA between the A30·T4 base pair and G28 base. (D) Halogen bond between OTA and the C5 base. The distance stands for the perpendicular distance from the chlorine atom to the aromatic ring. (E) Side view showing the hydrophobic interaction between the benzene ring of OTA and sugar ring of A27 and G28 and between the methyl group of the isocoumarin ring of OTA and the sugar ring of C29. The hydrogen and halogen bonds are shown as dashed lines. Oxygen, nitrogen, chlorine, and hydrogen atoms are depicted in red, blue, cyan, and gray, respectively.

the C5 base with the statistic mean distance of 3.2 Å and angle of 26° for 10 computed structures (Figure 6D). The chlorine atom of OTA attacks the nucleobases from above the aromatic ring of C5; such an X-bond with superb geometric characteristics is rare in nucleic acid complexes, and the geometry also suggests that the interaction of the halogen contributes strongly to the complex stability.

Upon complex formation, C29 does not stack with other bases, but forms the base quartet G6·T15·A27·C29 via its NH_2 group by twisting down the base (Figure 6A,B). The hydrophobic side (at positions 5 and 6 of the cytosine) of C29 turns away from the water solvent toward the molecule's interior, and the hydrophilic side moves toward the outside, which are supported by many NOEs between C29 and A27/G28/OTA (for instance, the NOEs between the methyl group of OTA and H2′/H2″/H3′/H5/H6 of C29 shown in Table S4). This special location of C29 not only contributes to its interaction with the methyl group of the isocoumarin ring of OTA by hydrophobicity but also benefits to close the binding pocket (Figure 6E).

In addition, the benzene ring of OTA also interacts by a hydrophobic effect with sugar rings of A27 and G28. We observed a series of NOEs between the benzene ring of OTA and the sugar rings of A27 and G28 and H8 of G28 (Figure 6E). Especially, H8 and H1′ protons of G28, which are positioned below the benzene ring of OTA, exhibit unusually upfield-shifted resonances (δ_{H8} 5.74 ppm and $\delta_{H1'}$ 4.54 ppm shown in Table S2) due to the shielding effect of the benzene ring of OTA.

The base quartet G6·T15·A27·C29 and triplet C5·T15·G28 provide important structural components to the architecture of the binding pocket. The base quartet/triplet alignments make these bases effectively fixed in the right position, respectively, greatly facilitating the stacking of the G28 base and isocoumarin ring of OTA, halogen bond formation between the aromatic ring of the C5 base and the chlorine atom of OTA, and the hydrophobic interaction between the sugar rings of A27 and G28 and the aromatic ring of OTA and between C29 and the methyl group of OTA.

Structural Insights into Discriminatory Recognition. OTA and OTB can be discriminately recognized by aptamers, although the only difference between OTA and OTB is that the chlorine in the isocoumarin ring of OTA is a hydrogen in OTB.[24] As shown in Figure S5, the 1D ^{1}H NMR spectra show that all imino protons in the OBA33−OTB complex gave rise to almost the same resonances to corresponding protons of the OBA33−OTA complex except the imino proton of G28 in the binding pocket and the NH proton of bound OTB. The NOESY spectra indicate that the intermolecular NOEs between OTB and OBA33 are also almost identical to those between OTA and OBA33, although the chemical shifts of protons from residues T4, C5, and G28 in the binding pocket shift compared to the OBA33−OTA complex (Figure S5 and Tables S4 and S5). These data indicate that OTA and OTB possess almost identical binding pockets when bound to aptamers but have remarkably different affinities. The only reasonable explanation is the formation of halogen bonds between the chlorine atom of OTA and the aptamer. The binding affinity of OBA33 is 54 nM for OTA and 17 μM for OTB (Figure S5), and the free energy of binding is −9.9 and −7.2 kcal mol^{-1}, respectively, meaning that the halogen bonds contribute 34% of the favorable free energy. The results suggest that the halogen bonds play a vital role in the aptamer discriminatory recognition of OTA and OTB.

DISCUSSION

Base Pair, Triple, and Quartet Alignment and the OBA−OTA Complex. The OBA33/OBA32−OTA complex structures are mainly composed of a double helix formed by

https://doi.org/10.1021/jacs.2c00478
J. Am. Chem. Soc. 2022, 144, 7731−7740

Watson−Crick pairs, a G-quadruplex formed by Hoogsteen pairs, and the OTA binding pocket containing base triple and quartet alignment. Most of base pair/triple/quartet in complex structures are formed by the participation of the G base because OBA33/OBA32 aptamers are G-rich. Therefore, we investigated the effect of the deletion of hydrogen bonds formed by the NH_2-2 group of the G base on the OBA32−OTA complex structure by the replacement of G with inosine (Figure S6 and Table S6). The imino ^{1}H NMR spectra indicate that the replacements of G10 and G28 cause a pronounced impact on the formation of the complex. The replacement of G10 with inosine results in the resonances of the G-quadruplex region significantly broadening, while the double-helix region is hardly affected, suggesting that the replacement seriously affects the stability of the G-quadruplex structure and further affects the binding to OTA. In the OBA32−OTA complex structures, G10 in the first 3-nt loop forms a G10·G24·C18 triple through its NH and NH_2-2 groups with N7 and the O6 carbonyl of the G24-C18 Watson−Crick pair in the third 7-nt loop, respectively (Figure 3), and thus the above observation also explains the important role of the G10·G24·C18 triple between two loops in stabilizing the G-quadruplex. The replacement of G28 with inosine induces an obvious increase in the number of resonance peaks, suggesting that the replacement seriously decreases the stability of the complex structure and probably leads to the coexistence of not less than two conformations. In the OBA32−OTA complex structures, G28 forms a G28·T15·C5 base triple through its NH and NH_2-2 groups with the O2 carbonyl of T15 and C5, respectively, which is deduced from the high-resolution OBA33−OTA complex structure. The triple alignment makes G28 fixed in the right position easy for the stacking of OTA. The removal of the NH_2-2 group destabilizes the G28·T15·C5 base triple and thus directly affects the binding of OTA.

In the OBA33−OTA 3D structure, the base quartet G6·T15·A27·C29 formed via hydrogen bonds is the important structural component of the ligand-binding pocket. The importance of this base quartet structure was also verified by base mutations. We replaced A27 with its isomer 2-aminopurine (2AP) (OBA33-27-AP), which will destroy the hydrogen bonds between the A27 base and the G6 and C29 bases due to exchanging the position of the NH_2 group. FP results indicate seriously decreased binding affinity (K_d: 1053 ± 48 nM) (Table S1 and Figure S3). We also replaced C29 with 5-methylcytosine (5mC) (OBA33-29-5mC), which probably impedes the forming of a hydrogen bond or destabilizes the ydrogen bond between NH_2 of C29 and N3 of A27 due to the steric effect of a methyl group to decrease the ligand-binding affinity, and meanwhile the hydrophobic interaction between OTA and C29 may enhance and thus increase the ligand-binding affinity. FP results also show the decreased binding affinity (K_d: 472 ± 17 nM) (Table S1 and Figure S3), suggesting the importance of the base quartet on complex formation.

We also investigated the effect of the duplex structure component on the OBA33 aptamer binding affinity to OTA by base mutations (Figure S3 and Table S1). We mutated A3·T31 to C3·G31 base pairs (OBA33-C3), and FP affinity determination shows the mutation hardly affects the binding to OTA (K_d: 61 ± 2 nM). However, the further mutation of T4·A30 to G4·C30 base pairs based on OBA33-C3 (OBA33-C3G4) results in remarkably decreased binding affinity to OTA (K_d: 1736 ± 63 nM), which is probably due to the fact that the T4·A30 base pair directly interacts with the isocoumarin ring of OTA by the $\pi-\pi$ stacking, and the G·C base pair does not stack well with OTA compared to the T·A base pair. Meanwhile, the hydrophobic interaction of methyl group of T4 with H9 of the isocoumarin ring of OTA, which was supported by strong NOE cross-peaks between methyl and H9 protons (Table S4), possibly contributes to the binding of aptamer to OTA. The hydrophobic interaction was destroyed due to the mutation of T4·A30 to G4·C30 base pairs, and thus the binding affinity decreased. The above observation indicates the important contribution of the T4·A30 stacking interaction with OTA to the strong binding affinity of the aptamer.

We have previously shown that stabilization of the OBA18 terminus by adding a GC base pair increased its binding affinity to OTA.[36] We wonder how the extension or truncation of a G−C base pair to the terminus of OBA33-C3 (OBA35) affects its affinity to OTA (Figure S3 and Table S1). FP data indicate OBA35 has a slightly increased affinity (K_d: 35 ± 4 nM). By contrast, the truncation of one G−C base pair on the terminus of OBA33 (OBA31) decreased the affinity (K_d: 141 ± 7 nM), and OBA29 with one more G−C base pair truncated in the duplex had greatly reduced affinity (K_d: 11.3 ± 0.6 μM) (Figure S3 and Table S1), in agreement with a previous report,[25] indicating that the stabilization of the duplex structure is important for the aptamer to maintain strong binding affinity.

Role of Metal Ions in Aptamer Recognition. In Mg^{2+}/Na^+/K^+ ternary ion buffer (Mg^{2+}: 10 mM, Na^+: 120 mM, and K^+: 5 mM), the aptamer forms an antiparallel G-quadruplex and duplex structure. In order to elucidate which of these ions stabilizes the structure of the aptamer, we acquired ^{1}H NMR spectra of OBA33 in buffer with different ions (Figure S7). It was found that the imino protons of OBA33 in Mg^{2+}/Na^+/K^+ ternary ion buffer gave rise to the same NMR spectra as that in Mg^{2+}/Na^+ binary ion buffer (Mg^{2+}: 10 mM and Na^+: 120 mM), different from the NMR spectra in Mg^{2+}/K^+ binary ion buffer (Mg^{2+}: 10 mM and K^+: 5 mM) and Mg^{2+} buffer (Mg^{2+}: 10 mM), both for free and bound aptamer (Figure S7A), suggesting that both Mg^{2+} and Na^+ ions in ternary ion buffer play an important role in stabilizing the structure of both free and bound aptamers. FP affinity assays show that Mg^{2+}/K^+ binary ions can also induce significant binding of OBA33, and the K_d is 77 ± 5 nM, a little bit larger than that in Mg^{2+}/Na^+ buffer (46 ± 2 nM) (Figure S7B), meaning K^+ and Na^+ have a similar function in aptamer binding with OTA and only one is needed in buffer. CD spectra in the absence of OTA confirm the existence of an antiparallel G-quadruplex conformation of OBA33 in Mg^{2+}/K^+ buffer or Mg^{2+}/Na^+ buffer, showing both K^+ and Na^+ help to stabilize the G-quadruplex, which is consistent with a previous report.[40] However, in the presence of OTA, OBA33 has a relatively more stable conformation in Mg^{2+}/Na^+ buffer and Mg^{2+}/Na^+/K^+ buffer than in Mg^{2+}/K^+ buffer (Figure S7C). In Mg^{2+}/Na^+/K^+ buffer, Na^+ (120 mM) has a much higher concentration than K^+ (5 mM), and Na^+ becomes a major component for structure stabilization. In addition, it was also found that the OBA33 aptamer at high concentrations (>0.3 mM) precipitates easily in the presence of OTA in Mg^{2+}/K^+ binary ion buffer, indicating that the aptamer is less stable in Mg^{2+}/K^+ than Mg^{2+}/Na^+ binary ion buffer.

The OBA33−OTA complex structure indicates that the negatively charged carboxyl and dissociated Ph-OH of OTA

https://doi.org/10.1021/jacs.2c00478
J. Am. Chem. Soc. 2022, 144, 7731−7740

are close to the negatively charged phosphate group of C29 and A30 within the binding pocket, and the high negative charge density is extremely unfavorable to the stability of the complex (Figure S8). Moreover, OTA prefers to form a Mg^{2+}-OTA complex with Mg^{2+} by Mg^{2+} binding to the oxygen atoms or to the aromatic rings.[41] We speculated that Mg^{2+} ions affect the binding of OTA to the aptamer mainly by directly influencing the form of the binding pocket. Therefore, we investigated the effect of Mg^{2+} on the imino protons of OBA33 by NMR titration experiment in the presence of OTA in buffer containing 120 mM NaCl (pH 7.5) at 288 K (Figure S9). We observed that the resonances of imino protons of T4, T15, and G28 bases from the binding pocket and NH proton from bound OTA shift with the increase of Mg^{2+} concentration, demonstrating the coordination of Mg^{2+} exists in the aptamer−OTA complex, which plays a crucial role in stabilizing the complex structure.

In short, Mg^{2+} and Na^{+} ions induce the aptamer to form a flexible and less well-defined duplex and antiparallel G-quadruplex structures, providing a structural scaffold for the binding of OTA. In the presence of OTA, the aptamer is induced to form a compact binding pocket by halogen bonding, $\pi-\pi$ stacking, and hydrophobic interactions, which makes a tightly stacked and stable overall structure of the aptamer−OTA complex form.

Structure Comparison. We have previously solved the solution high-resolution structure of OTA bound to the 19-mer aptamer (OBA3−OTA complex) with weak affinity at the μM level.[36] The determination of the high-resolution structure of the OBA33−OTA complex offers us the opportunity to compare these two aptamers with distinct affinities to OTA. The OBA3−OTA complex forms a hairpin structure containing an intramolecular triple helix, and the OTA inserts between the G5·C11 base pair and G12·G4·C16 triple to form a sandwich structure, mainly interacting by stacking with bases and halogen bonding (Figure S10). While the OBA33−OTA complex folds into a duplex−quadruplex structural scaffold, the OTA is surrounded by the A30·T4 base pair and the bases C5, G28, C29, and T15, interacting by stacking with bases, a halogen bond, and a hydrophobic effect, to form a pocket-like structure, which provides more surface area contact than the OTA binding site in OBA3. The strength of the halogen bond depends not only on the chemical donor−acceptor combination but also on the bond lengths and bond angles. The halogen bonds between G5 N7/N9/O6 atoms and the chlorine of OTA are weak within the binding pocket of the OBA3−OTA complex, and the mean distances and angles are 3.9 Å/135°, 3.95 Å/112°, and 4.19 Å/111°, respectively. While the relatively strong halogen bond formation between the chlorine atom of OTA and the aromatic ring of C5 within the binding pocket of the OBA33−OTA complex, the statistical mean perpendicular distance between the halogen atom and the aromatic ring plane and the mean angle between the R−X bond and plane normal vector are 3.2 Å and 26° for 10 computed structures, respectively. The differences above are probably the major reason that OBA33 has a relatively high binding affinity compared to OBA3.

We note that many small-molecule DNA/RNA complexes fold into duplex−quadruplex structures,[42] such as quadruplex−duplex junction−ligand complexes,[43−46] and fluorogenic RNA aptamer−ligand complexes.[47−53] However, the interaction mode between DNA/RNA and the ligand in these complexes is different from that in the OBA33−OTA complex. G-Quadruplexes in these complexes are directly involved in the DNA/RNA−ligand interaction through the stacking interaction between the ligand and the G-quartet layer. However, OTA especially binds to the junction region between the double helix and G-quadruplex through halogen bonds, $\pi-\pi$ stacking, and hydrophobic interactions and lacks direct contacts with the G-quadruplex in the OBA33−OTA complex, which provides a new aptamer-binding motif.

CONCLUSION

In conclusion, we determined the high-resolution structure of OTA bound to the high-affinity 33-mer aptamer (OBA33−OTA complex) by solution NMR spectroscopy, by which we reveal the specific molecular recognition mechanism of the widely used G-rich OTA aptamer OBA36 and its truncated aptamers. The aptamer folds into a less well-defined duplex−G-quadruplex structure scaffold similar to a ligand-bound complex in the presence of Mg^{2+} and Na^{+} ions. The insertion of OTA induces binding pocket formation and thus the tightly stacked well-defined overall structure of complex forms. OTA does not directly contact the G-quadruplex, whereas it binds at the junction between the double helix and G-quadruplex through stacking, halogen bonding, and hydrophobic interactions. The halogen bonds between OTA and the aptamer base play a key role in target discriminating and strong binding. Our work contributes to the deep understanding of a specific OTA aptamer recognition mechanism for high affinity binding and also provides a basis for design and improvement of the OTA aptamer and aptamer-based biosensor.

ASSOCIATED CONTENT

Supporting Information

The Supporting Information is available free of charge at https://pubs.acs.org/doi/10.1021/jacs.2c00478.

NMR spectra, fluorescence polarization titration, sequence and dissociation constant of aptamers, proton chemical shift, statistics of the computed structures, intermolecular NOE data, including Tables S1−S6 and Figures S1−S10 (PDF)

Accession Codes

The coordinates for the OBA33−OTA complex have been deposited in the Protein Data Bank (accession number: 7W9N).

AUTHOR INFORMATION

Corresponding Authors

Conggang Li − *Key Laboratory of Magnetic Resonance in Biological Systems, State Key Laboratory of Magnetic Resonance and Atomic and Molecular Physics, National Center for Magnetic Resonance in Wuhan, Wuhan National Laboratory for Optoelectronics, Wuhan Institute of Physics and Mathematics, Innovation Academy for Precision Measurement Science and Technology, Chinese Academy of Sciences, Wuhan 430071, People's Republic of China;* orcid.org/0000-0002-5798-1722; Email: congganli@wipm.ac.cn

Qiang Zhao − *State Key Laboratory of Environmental Chemistry and Ecotoxicology, Research Center for Eco-Environmental Sciences, Chinese Academy of Sciences, Beijing 100085, People's Republic of China; Hangzhou Institute for Advanced Study, UCAS, Hangzhou 310000, People's Republic of China; University of Chinese Academy of*

https://doi.org/10.1021/jacs.2c00478
J. Am. Chem. Soc. 2022, 144, 7731−7740

Sciences, Beijing 100049, People's Republic of China; orcid.org/0000-0003-3448-8756; Email: qiangzhao@rcees.ac.cn

Authors

Guohua Xu − *Key Laboratory of Magnetic Resonance in Biological Systems, State Key Laboratory of Magnetic Resonance and Atomic and Molecular Physics, National Center for Magnetic Resonance in Wuhan, Wuhan National Laboratory for Optoelectronics, Wuhan Institute of Physics and Mathematics, Innovation Academy for Precision Measurement Science and Technology, Chinese Academy of Sciences, Wuhan 430071, People's Republic of China*

Jiajing Zhao − *Key Laboratory of Magnetic Resonance in Biological Systems, State Key Laboratory of Magnetic Resonance and Atomic and Molecular Physics, National Center for Magnetic Resonance in Wuhan, Wuhan National Laboratory for Optoelectronics, Wuhan Institute of Physics and Mathematics, Innovation Academy for Precision Measurement Science and Technology, Chinese Academy of Sciences, Wuhan 430071, People's Republic of China; Xi'an Modern Chemistry Research Institute, Xi'an 710065, People's Republic of China*

Hao Yu − *State Key Laboratory of Environmental Chemistry and Ecotoxicology, Research Center for Eco-Environmental Sciences, Chinese Academy of Sciences, Beijing 100085, People's Republic of China; University of Chinese Academy of Sciences, Beijing 100049, People's Republic of China*

Chen Wang − *Key Laboratory of Magnetic Resonance in Biological Systems, State Key Laboratory of Magnetic Resonance and Atomic and Molecular Physics, National Center for Magnetic Resonance in Wuhan, Wuhan National Laboratory for Optoelectronics, Wuhan Institute of Physics and Mathematics, Innovation Academy for Precision Measurement Science and Technology, Chinese Academy of Sciences, Wuhan 430071, People's Republic of China; University of Chinese Academy of Sciences, Beijing 100049, People's Republic of China*

Yangyu Huang − *Shaoyang University, Shaoyang 422000, People's Republic of China*

Xin Zhou − *Key Laboratory of Magnetic Resonance in Biological Systems, State Key Laboratory of Magnetic Resonance and Atomic and Molecular Physics, National Center for Magnetic Resonance in Wuhan, Wuhan National Laboratory for Optoelectronics, Wuhan Institute of Physics and Mathematics, Innovation Academy for Precision Measurement Science and Technology, Chinese Academy of Sciences, Wuhan 430071, People's Republic of China;* orcid.org/0000-0002-5580-7907

Maili Liu − *Key Laboratory of Magnetic Resonance in Biological Systems, State Key Laboratory of Magnetic Resonance and Atomic and Molecular Physics, National Center for Magnetic Resonance in Wuhan, Wuhan National Laboratory for Optoelectronics, Wuhan Institute of Physics and Mathematics, Innovation Academy for Precision Measurement Science and Technology, Chinese Academy of Sciences, Wuhan 430071, People's Republic of China;* orcid.org/0000-0002-9359-915X

Complete contact information is available at: https://pubs.acs.org/10.1021/jacs.2c00478

Notes

The authors declare no competing financial interest.

■ ACKNOWLEDGMENTS

This work is supported by National Natural Science Foundation of China grants (21925406, 21874149, 21921004, 21874146, 22074156) and Ministry of Science and Technology of China grant [2017YFA0505400].

■ REFERENCES

(1) Tuerk, C.; Gold, L. Systematic evolution of ligands by exponential enrichment - RNA ligands to bacteriophage-T4 DNA-polymerase. *Science* **1990**, *249*, 505−510.

(2) Ellington, A. D.; Szostak, J. W. In vitro selection of RNA molecules that bind specific ligands. *Nature* **1990**, *346*, 818−822.

(3) Yu, H. X.; Alkhamis, O.; Canoura, J.; Liu, Y. Z.; Xiao, Y. Advances and challenges in small-molecule DNA aptamer isolation, characterization, and sensor development. *Angew. Chem., Int. Ed.* **2021**, *60*, 16800−16823.

(4) Dunn, M. R.; Jimenez, R. M.; Chaput, J. C. Analysis of aptamer discovery and technology. *Nat. Rev. Chem.* **2017**, *1*, 0076.

(5) Wu, L. L.; Wang, Y. D.; Xu, X.; Liu, Y. L.; Lin, B. Q.; Zhang, M. X.; Zhang, J. L.; Wan, S.; Yang, C. Y.; Tan, W. H. Aptamer-based detection of circulating targets for precision medicine. *Chem. Rev.* **2021**, *121*, 12035−12105.

(6) Sun, M.; Liu, S.; Song, T.; Chen, F.; Zhang, J.; Huang, J. A.; Wan, S.; Lu, Y.; Chen, H.; Tan, W.; Song, Y.; Yang, C. Spherical neutralizing aptamer inhibits SARS-CoV-2 infection and suppresses mutational escape. *J. Am. Chem. Soc.* **2021**, *143*, 21541−21548.

(7) Zhang, Z. J.; Pandey, R.; Li, J. X.; Gu, J.; White, D.; Stacey, H. D.; Ang, J. C.; Steinberg, C. J.; Capretta, A.; Filipe, C. D. M.; Mossman, K.; Balion, C.; Miller, M. S.; Salena, B. J.; Yamamura, D.; Soleymani, L.; Brennan, J. D.; Li, Y. F. High-affinity dimeric aptamers enable the rapid electrochemical detection of wild-type and B.1.1.7 SARS-CoV-2 in unprocessed saliva. *Angew. Chem., Int. Ed.* **2021**, *60*, 24266−24274.

(8) Zhou, J. H.; Rossi, J. Aptamers as targeted therapeutics: current potential and challenges. *Nat. Rev. Drug. Discovery* **2017**, *16*, 440−440.

(9) Nutiu, R.; Li, Y. F. Structure-switching signaling aptamers. *J. Am. Chem. Soc.* **2003**, *125*, 4771−4778.

(10) Lacroix, A.; Sleiman, H. F. DNA nanostructures: Current challenges and opportunities for cellular delivery. *ACS Nano* **2021**, *15*, 3631−3645.

(11) Canoura, J.; Wang, Z. W.; Yu, H. X.; Alkhamis, O.; Fu, F. F.; Xiao, Y. No structure-switching required: A generalizable exonuclease-mediated aptamer-based assay for small-molecule detection. *J. Am. Chem. Soc.* **2018**, *140*, 9961−9971.

(12) Sharma, A. K.; Heemstra, J. M. Small-molecule-dependent split aptamer ligation. *J. Am. Chem. Soc.* **2011**, *133*, 12426−12429.

(13) Zuo, X. L.; Xiao, Y.; Plaxco, K. W. High specificity, electrochemical sandwich assays based on single aptamer sequences and suitable for the direct detection of small-molecule targets in blood and other complex matrices. *J. Am. Chem. Soc.* **2009**, *131*, 6944−6945.

(14) Wang, K. B.; Dickerhoff, J.; Wu, G. H.; Yang, D. Z. PDGFR-beta promoter forms a vacancy G-quadruplex that can be filled in by dGMP: Solution structure and molecular recognition of guanine metabolites and drugs. *J. Am. Chem. Soc.* **2020**, *142*, 5204−5211.

(15) Hermann, T.; Patel, D. J. Biochemistry - Adaptive recognition by nucleic acid aptamers. *Science* **2000**, *287*, 820−825.

(16) Bottari, F.; Daems, E.; de Vries, A. M.; Van Wielendaele, P.; Trashin, S.; Blust, R.; Sobott, F.; Madder, A.; Martins, J. C.; De Wael, K. Do aptamers always bind? The need for a multifaceted analytical approach when demonstrating binding affinity between aptamer and low molecular weight compounds. *J. Am. Chem. Soc.* **2020**, *142*, 19622−19630.

(17) Nakatsuka, N.; Yang, K. A.; Abendroth, J. M.; Cheung, K. M.; Xu, X. B.; Yang, H. Y.; Zhao, C. Z.; Zhu, B. W.; Rim, Y. S.; Yang, Y.; Weiss, P. S.; Stojanovic, M. N.; Andrews, A. M. Aptamer-field-effect transistors overcome Debye length limitations for small-molecule sensing. *Science* **2018**, *362*, 319−324.

(18) Pfohl-Leszkowicz, A.; Manderville, R. A. Ochratoxin A: An overview on toxicity and carcinogenicity in animals and humans. *Mol. Nutr. Food Res.* **2007**, *51*, 61−99.
(19) Bui-Klimke, T. R.; Wu, F. Ochratoxin A and human health risk: A review of the evidence. *Crit. Rev. Food Sci.* **2015**, *55*, 1860−1869.
(20) Khoi, C. S.; Chen, J. H.; Lin, T. Y.; Chiang, C. K.; Hung, K. Y. Ochratoxin A-induced nephrotoxicity: Up-to-date evidence. *Int. J. Mol. Sci.* **2021**, *22*, 11237.
(21) Bostan, H. B.; Danesh, N. M.; Karimi, G.; Ramezani, M.; Shaegh, S. A. M.; Youssefi, K.; Charbgoo, F.; Abnous, K.; Taghdisi, S. M. Ultrasensitive detection of ochratoxin A using aptasensors. *Biosens. Bioelectron.* **2017**, *98*, 168−179.
(22) Nao, S. C.; Wu, K. J.; Wang, W. H.; Leung, C. H.; Ma, D. L. Recent progress and development of G-quadruplex-based luminescent assays for Ochratoxin A detection. *Front. Chem.* **2020**, *8*, 767.
(23) Guo, X. D.; Wen, F.; Zheng, N.; Saive, M.; Fauconnier, M. L.; Wang, J. Q. Aptamer-based biosensor for detection of mycotoxins. *Front. Chem.* **2020**, *8*, 195.
(24) Cruz-Aguado, J. A.; Penner, G. Determination of Ochratoxin A with a DNA aptamer. *J. Agr. Food Chem.* **2008**, *56*, 10456−10461.
(25) Geng, X.; Zhang, D. P.; Wang, H. L.; Zhao, Q. Screening interaction between ochratoxin A and aptamers by fluorescence anisotropy approach. *Anal. Bioanal. Chem.* **2013**, *405*, 2443−2449.
(26) Yang, C.; Wang, Y.; Marty, J. L.; Yang, X. R. Aptamer-based colorimetric biosensing of Ochratoxin A using unmodified gold nanoparticles indicator. *Biosens. Bioelectron.* **2011**, *26*, 2724−2727.
(27) Deore, P. S.; Gray, M. D.; Chung, A. J.; Manderville, R. A. Ligand-induced G-quadruplex polymorphism: A DNA nanodevice for label-free aptasensor platforms. *J. Am. Chem. Soc.* **2019**, *141*, 14288−14297.
(28) Fadock, K. L.; Manderville, R. A. DNA Aptamer-target binding motif revealed using a fluorescent guanine probe: Implications for food toxin detection. *ACS Omega* **2017**, *2*, 4955−4963.
(29) Phan, A. T. Long-range imino proton-C13 J-couplings and the through-bond correlation of imino and non-exchangeable protons in unlabeled DNA. *J. Biomol. NMR* **2000**, *16*, 175−178.
(30) Sklenar, V.; Miyashiro, H.; Zon, G.; Miles, H. T.; Bax, A. Assignment of the P-31 and H-1 resonances in oligonucleotides by two-dimensional NMR-spectroscopy. *FEBS Lett.* **1986**, *208*, 94−98.
(31) Luy, B.; Marino, J. P. H-1-P-31 CPMG-correlated experiments for the assignment of nucleic acids. *J. Am. Chem. Soc.* **2001**, *123*, 11306−11307.
(32) Goddard, T.; Kneller, D. *SPARKY*; University of California, San Francisco, 2001.
(33) Bermejo, G. A.; Clore, G. M.; Schwieters, C. D. Improving NMR structures of RNA. *Structure* **2016**, *24*, 806−815.
(34) Schwieters, C. D.; Kuszewski, J. J.; Tjandra, N.; Clore, G. M. The Xplor-NIH NMR molecular structure determination package. *J. Magn. Reson.* **2003**, *160*, 65−73.
(35) Schwieters, C. D.; Kuszewski, J. J.; Clore, G. M. Using Xplor-NIH for NMR molecular structure determination. *Prog. Nucl. Mag. Res. Sp.* **2006**, *48*, 47−62.
(36) Xu, G. H.; Zhao, J. J.; Liu, N.; Yang, M. H.; Zhao, Q.; Li, C. G.; Liu, M. L. Structure-guided post-SELEX optimization of an ochratoxin A aptamer. *Nucleic Acids Res.* **2019**, *47*, 5963−5972.
(37) Adrian, M.; Heddi, B.; Phan, A. T. NMR spectroscopy of G-quadruplexes. *Methods* **2012**, *57*, 11−24.
(38) Kolar, M. H.; Tabarrini, O. Halogen bonding in nucleic acid complexes. *J. Med. Chem.* **2017**, *60*, 8681−8690.
(39) Cavallo, G.; Metrangolo, P.; Milani, R.; Pilati, T.; Priimagi, A.; Resnati, G.; Terraneo, G. The halogen bond. *Chem. Rev.* **2016**, *116*, 2478−2601.
(40) Bhattacharyya, D.; Arachchilage, G. M.; Basu, S. Metal cations in G-quadruplex folding and stability. *Front. Chem.* **2016**, *4*, 38.
(41) Poor, M.; Kunsagi-Mate, S.; Matisz, G.; Li, Y.; Czibulya, Z.; Peles-Lemli, B.; Koszegi, T. Interaction of alkali and alkaline earth ions with Ochratoxin A. *J. Lumin.* **2013**, *135*, 276−280.
(42) Kotkowiak, W.; Pasternak, A. Beyond G-quadruplexes—the effect of junction with additional structural motifs on aptamers properties. *Int. J. Mol. Sci.* **2021**, *22*, 9948.
(43) Vianney, Y. M.; Weisz, K. Indoloquinoline ligands favor intercalation at quadruplex-duplex interfaces. *Chem.—Eur. J.* **2020**, *28*, No. e202103718.
(44) Vianney, Y. M.; Preckwinkel, P.; Mohr, S.; Weisz, K. Quadruplex-duplex junction: A high-affinity binding site for indoloquinoline ligands. *Chem.—Eur. J.* **2020**, *26*, 16910−16922.
(45) Diaz-Casado, L.; Serrano-Chacon, I.; Montalvillo-Jimenez, L.; Corzana, F.; Bastida, A.; Santana, A. G.; Gonzalez, C.; Asensio, J. L. De Novo design of selective quadruplex-duplex junction ligands and structural characterisation of their binding mode: targeting the G4 hot-spot. *Chem.—Eur. J.* **2021**, *27*, 6204−6212.
(46) Liu, L. Y.; Wang, K. N.; Liu, W. T.; Zeng, Y. L.; Hou, M. X.; Yang, J.; Mao, Z. W. Spatial matching selectivity and solution structure of organic-metal hybrid to quadruplex-duplex hybrid. *Angew. Chem., Int. Ed.* **2021**, *38*, 20833−20839.
(47) Paige, J. S.; Nguyen-Duc, T.; Song, W. J.; Jaffrey, S. R. Fluorescence imaging of cellular metabolites with RNA. *Science* **2012**, *335*, 1194−1194.
(48) Warner, K. D.; Chen, M. C.; Song, W. J.; Strack, R. L.; Thorn, A.; Jaffrey, S. R.; Ferre-D'Amare, A. R. Structural basis for activity of highly efficient RNA mimics of green fluorescent protein. *Nat. Struct. Mol. Biol.* **2014**, *21*, 658−663.
(49) Huang, H.; Suslov, N. B.; Li, N. S.; Shelke, S. A.; Evans, M. E.; Koldobskaya, Y.; Rice, P. A.; Piccirilli, J. A. A G-quadruplex-containing RNA activates fluorescence in a GFP-like fluorophore. *Nat. Chem. Biol.* **2014**, *10*, 686−691.
(50) Mieczkowski, M.; Steinmetzger, C.; Bessi, I.; Lenz, A. K.; Schmiedel, A.; Holzapfel, M.; Lambert, C.; Pena, V.; Hobartner, C. Large Stokes shift fluorescence activation in an RNA aptamer by intermolecular proton transfer to guanine. *Nat. Commun.* **2021**, *12*, 3549.
(51) Warner, K. D.; Sjekloca, L.; Song, W. J.; Filonov, G. S.; Jaffrey, S. R.; Ferre-D'Amare, A. R. A homodimer interface without base pairs in an RNA mimic of red fluorescent protein. *Nat. Chem. Biol.* **2017**, *13*, 1195−1201.
(52) Trachman, R. J.; Demeshkina, N. A.; Lau, M. W. L.; Panchapakesan, S. S. S.; Jeng, S. C. Y.; Unrau, P. J.; Ferre-D'Amare, A. R. Structural basis for high-affinity fluorophore binding and activation by RNA Mango. *Nat. Chem. Biol.* **2017**, *13*, 807−813.
(53) Trachman, R. J.; Autour, A.; Jeng, S. C. Y.; Abdolahzadeh, A.; Andreoni, A.; Cojocaru, R.; Garipov, R.; Dolgosheina, E. V.; Knutson, J. R.; Ryckelynck, M.; Unrau, P. J.; Ferre-D'Amare, A. R. Structure and functional reselection of the Mango-III fluorogenic RNA aptamer. *Nat. Chem. Biol.* **2019**, *15*, 472−479.

https://doi.org/10.1021/jacs.2c00478
J. Am. Chem. Soc. 2022, 144, 7731−7740